Sheffield Hallam University

Optical and structural properties of d0 ion-doped silicate glasses for photovoltaic applications

ALLSOPP, Benjamin, CHRISTOPOULOU, Georgina, BROOKFIELD, Adam, FORDER, Sue and BINGHAM, Paul <http://orcid.org/0000-0001-6017-0798>

Available from Sheffield Hallam University Research Archive (SHURA) at:

https://shura.shu.ac.uk/21052/

This document is the Accepted Version [AM]

Citation:

ALLSOPP, Benjamin, CHRISTOPOULOU, Georgina, BROOKFIELD, Adam, FORDER, Sue and BINGHAM, Paul (2018). Optical and structural properties of d0 ion-doped silicate glasses for photovoltaic applications. Physics and Chemistry of Glasses : European Journal of Glass Science and Technology Part B, 59 (4), 193-202. [Article]

Copyright and re-use policy

See http://shura.shu.ac.uk/information.html

Sheffield Hallam University Research Archive
http://shura.shu.ac.uk

Optical and structural properties of d^0 ion-doped silicate glasses for photovoltaic applications

Benjamin L. Allsopp[1], Georgia Christopoulou[1], Adam Brookfield[2], Susan D. Forder[1] and Paul A. Bingham[1*]

[1] *Materials and Engineering Research Institute, Faculty of Arts, Computing, Engineering and Sciences, Sheffield Hallam University, City Campus, Howard Street, Sheffield, S1 1WB, UK*

[2] *EPR Facility, 2.315 Photon Science Institute, University of Manchester, Oxford Road, M13 9PL, UK*

Corresponding author email – P.A.Bingham@shu.ac.uk

Abstract

Optical and structural properties of float-type soda lime silicate (SLS) glasses doped with 0.2 mol % TiO_2, ZrO_2, HfO_2, Nb_2O_5, Ta_2O_5, MoO_3 or WO_3 have been studied. Under UV excitation all d^0 doped glasses exhibit broadband visible emission centred between 19,000 cm^{-1} and 25,000 cm^{-1} (400nm – 525nm) due to a transition from the 2*p* orbital of O^{2-} to the metal d^0 orbital. Dopant additions lead to shifts in the UV absorption edge to lower energies, with doped glasses having an absorption edge 2,000 cm^{-1} (~20nm), and in the case of MoO_3, 4,000 cm^{-1} (~40nm), lower than the corresponding undoped glass. Combined UV-Vis absorption and X-band EPR spectroscopy analyses confirm that dopant cations occur in the studied glasses in the expected oxidation states of Ti^{4+}, Zr^{4+}, Hf^{4+}, Nb^{5+}, Ta^{5+}, Mo^{6+} and W^{6+}, although very low levels of Mo^{5+} are also observed, as demonstrated by the EPR resonance at g=1.92 (3.7T). The incorporation of the studied dopants into SLS glasses may find applications as cover glasses in photovoltaic (PV) applications, providing UV protection of polymers and solar cell materials in PV units whilst enhancing solar cell efficiency through downconversion / fluorescence of absorbed UV photons with re-emission as visible photons, available for absorption and conversion by the solar cell material.

Key words: d^0 ion, visible fluorescence, silicate glass

1. Introduction

As solar energy contributes a growing proportion of the energy mix in many countries, there remains a worldwide drive to reduce the cost per Watt of photovoltaic (PV) energy [1]. There are three primary methods of achieving this: (i) increase the service lifetime of the PV cell or module; (ii) increase the efficiency of the PV cell or module; or (iii) decrease the total cell or module cost [2].

Figure 1 demonstrates a typical crystalline silicon (c-Si) solar cell module construction. This study focuses on modifying the SLS glass front sheet and thus the technology is also applicable to PV modules incorporating other cell materials such as amorphous silicon (a-Si), GaAs, CdS/CdTe, perovskite or dye sensitised solar cells. Various glues are utilised for the encapsulant layer, notably polyvinyl butyral (PVB), thermoplastic polyurethane (TPU), and ethylene vinyl acetate (EVA), whilst the back sheets are either aluminium or polyvinyl fluoride (e.g. Tedlar®) [3]. These backsheets are selected for a combination of aesthetics, protection from the environment and reflectivity.

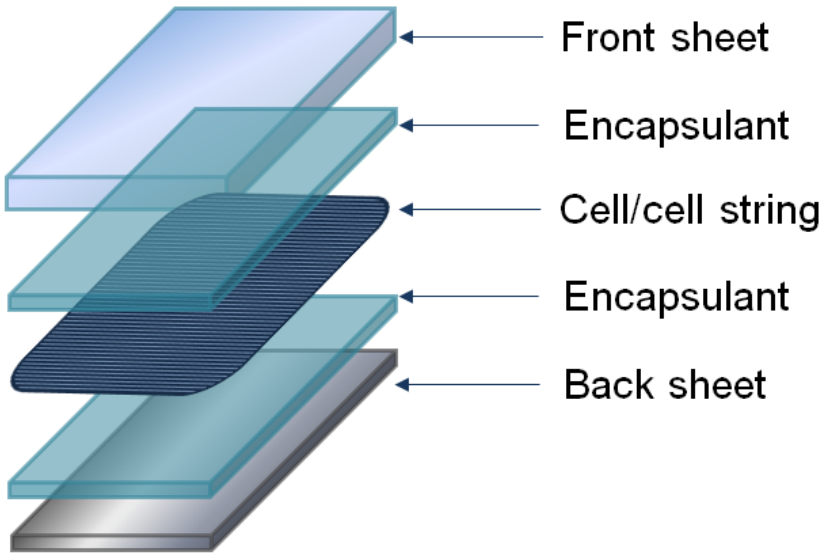

Figure 1. Typical c-Si solar cell construction (reproduced with permission - Solar Capture Technologies)

PV modules have a desired service lifetime of 20-30 years, however, in high-UV localities this may be substantially reduced due to polymeric damage [4]. During their service lifetimes, c-Si PV module performance degrades by 0.6 - 2.5% per year

depending on service conditions and manufacturer [4,5]. A major cause of failure within the expected service lifetime of PV modules is delamination caused by UV-induced degradation of the encapsulant layers and polymeric backsheets [3,6], allowing water to ingress and corrode the materials within [7]. Even before delamination occurs, the EVA layer can become discoloured, reducing light transmission and contributing to reduced module efficiency [8]. Absorption of damaging UV photons within the glass front sheet can thus increase the service lifetimes of PV modules. Whilst Fe^{2+} and Fe^{3+} in glass strongly shift the UV absorption towards the visible, beneficially protecting the polymeric layers from UV damage, there are also visible and IR absorptions which parasitically absorb photons that could otherwise be converted by the photovoltaic material. Absorptions in the UV to visible from 27,250cm^{-1} (366nm) to 21,550cm^{-1} (464nm) corresponding to Fe^{3+}, and strong absorptions within the IR between 10,380cm^{-1} (963nm) and 7490cm^{-1} (1335nm) corresponding to Fe^{2+} [9], limit the effectiveness of doping with iron for solar control. Absorptions such as these from 0.01mol% Fe_2O_3 in silcate glass can cause a 1.1% loss in module output power, and a 9.8% loss for a 0.1mol% Fe_2O_3 doped silicate glass encapsulant [10]. Reduction of the concentration of Fe in glass is therefore a requirement to facilitate more effective photovoltaic panels, and this approach has been employed industrially. UV control for the protection of the polymeric materials can be achieved through d^0 transition metal ions doped into the glass front sheet.

Absorption of high-energy UV photons can give two effects; (i) the energy converting to phonons (heat), (ii) fluorescence / downconversion to visible photons. To generate electrical current in a solar cell semiconductor an electron-hole pair must be generated by the absorption of photons equal or slightly greater in energy than the bandgap, in the case of silicon 1.11 eV. However, if the energy of the incoming photon is much greater than the bandgap energy, the excess energy is lost as heat which reduces solar cell efficiency [11]. Photons with energy lower than the bandgap energy cannot induce an electron hole pair. Since a single-junction silicon solar cell has a theoretical maximum limit of 30%, known as the Shockley-Quiesser limit [12], modification of the solar spectrum through downconversion, upconversion or fluorescence may be employed as a means of increasing the flux of photons with energies at or just above the bandgap

energy [13–15]. There are two related, but distinct, methods of converting higher energy UV photons to lower energy visible photons: photoluminescence and downconversion. Photoluminescence is characterised by a non-radiative step after excitation, leading to one photon of lower energy being emitted. Downconversion may have a quantum efficiency of greater than 1 as after excitation there is a stepwise radiative relaxation, resulting in two or more photons of lower energy being emitted. The two processes are schematically illustrated in Figure 2.

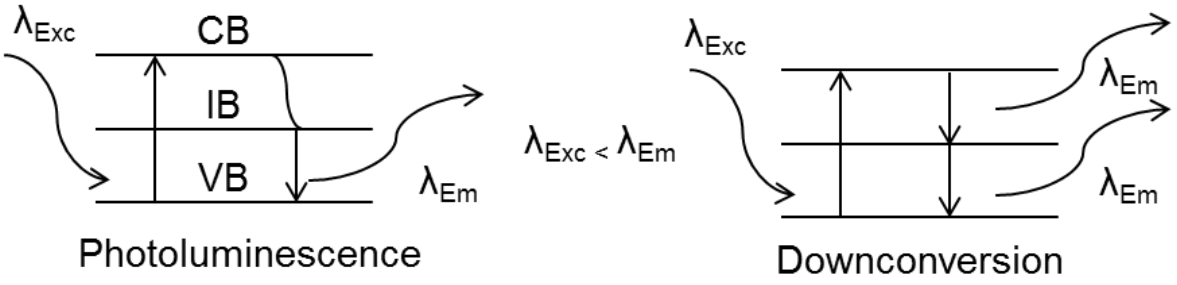

Figure 2. Schematic of photoluminescence and downconversion, CB = Conduction band, IB = Intermediate band, VB = Valance band

Some of the recent research in spectral modification for photovoltaics has been focussed on glasses doped with lanthanide elements [16–19]. This interest has been predominantly in upconversion of IR wavelengths to visible wavelengths. Transition metals are not normally used as dopants in PV module glasses as many transition metals produce *d-d* absorption bands at visible and near-IR energies, which would have a deleterious effect on solar cell efficiency. However, certain transition metals in certain oxidation states, specifically those with a d^0 configuration [20–22], have a full outer electron shell, which has traditionally been thought to hamper electronic transitions, and they produce no *d-d* absorption visible or near-IR bands [23,24] but fluoresce in the visible under UV excitation [25–27]. Consequently we hypothesised that such dopants may prove beneficial for doping PV module cover glasses, in that visible and near-IR absorption would be minimised whilst UV absorption would be increased; and the glasses may demonstrate downconversion or fluorescence at visible energies. Only a few studies [20–22,27] have investigated the phenomenon of downconversion and

fluorescence of d^0 ions in silicate glasses. There is extensive literature concerning d^0 fluorescence in crystalline materials [28–32] and other glass systems. However, glasses produced using a standard melt quench procedure doped with various d^0 transition metal ions have been demonstrated to fluoresce under UV excitation (Figure 10) [20]. The low doping levels used within this study potentially confer two benefits: (i) relatively low additional raw materials cost due to the low level of additions; and (ii) may enable technologically achievable melting in float glass plants due to minimal changes in composition. By modifying the cover glasses in PV modules, an efficiency increase can be envisaged, along with protecting the polymeric glues from UV light degradation. In this work, the optical and structural effects of adding small doping levels of d^0 transition metal ions in a representative soda-lime-silicate (SLS) float glass system have been investigated.

2. Experimental Methods

Raw materials of ≥ 99.9% purity of sand (SiO_2), alumina ($Al(OH)_3$), magnesium carbonate ($MgCO_3$), calcium carbonate ($CaCO_3$), sodium carbonate (Na_2CO_3), sodium sulphate (Na_2SO_4) and zinc oxide (ZnO) and iron oxide (Fe_2O_3) were dried at 110^{o}C for at least 24 hours to remove moisture, then weighed and mixed before melting. Batches to produce 100g of glass of the nominal compositions listed in Table 1 were melted in a zirconia grain stabilised platinum (ZGS-Pt) crucible at 1450^{0}C for 5 hours, before pouring into moulds on a steel plate and annealing at 530^{0}C for 1 hour then cooling within the furnace to room temperature to remove thermal stresses. Samples were polished with decreasing SiC grit sizes to 1µm, before a final polish of 1µm CeO_2 for optical measurements; all other measurements were carried out using powdered glass, prepared in a vibratory disc mill. A base glass was produced using the same method with the 0.20 mol% of dopant replaced by SiO_2. Three iron oxide doped glasses were produced with the doping levels of 0.01mol%, 0.05mol% and 0.10mol% Fe_2O_3, with the iron replacing SiO_2 as per the base glass.

X-ray diffraction (XRD) was carried out using a Philips X-Pert X-ray diffractometer, with Cu K_α radiation = 1.5405980Å, working at 40kV and 40mA on a spinner stage with a step size of 0.001 $^o2\theta$. Electron paramagnetic resonance (EPR) measurements were

obtained using a Brucker EMX Premium X EPR spectrometer. Powder samples were measured in silica capillary tubes at room temperature (20^{o}C) at X-Band frequencies (~9.80GHz). Magnetic power was adjusted to collect convenient signal-to-noise ratios without saturation. An empty capillary tube was also measured to enable background correction of sample spectra. EPR measurements were undertaken for qualitative purposes to determine the oxidation state of dopants preponderantly in d^0 configuration. UV-Vis absorption spectra were measured on a Varian Cary 50 scan UV visible spectrophotometer over the range 200-1000nm, at a scan rate of 60nm/min with a data interval of 0.5nm. Fluorescence measurements were collected on a Varian Cary Eclipse fluorescence spectrophotometer. Samples were held at 30^0 to the excitation source and scanned at 240nm to 330nm in 10nm intervals, with the 360-1100nm filter to remove excitation interference. All samples were scanned with 120nm/min scan rate, with a data interval of 1nm, and slit widths of 20nm for excitation and 20nm for emission; the detector voltage was set to 400V. The chemical composition of the prepared base glass was analysed using a Phillips Magix Pro X-Ray fluorescence spectrometer and a Panalytical Axios Fast fluorescence spectrometer in a 1:10 sample to lithium tetraborate flux ratio as a fused bead. Beads were melted in a Pt/5%Au crucible at 1065^{o}C for 15 minutes before being air cooled. Scans were carried out on the SuperQ 3-IQ+ software in the oxide setting. Uncertainties in XRF analysis results are conservatively estimated to be ±2% of the measured concentrations. Sample densities were measured on samples of 10-30g bulk glass using the Archimedes method in deionised water. Results shown in table 1 are averages of at least 3 independent measurements, corrected for the density of water at the measurement temperature. Uncertainties in measured densities are estimated to be ± 0.005 g cm^{-3}.

Table 1 Sample nominal and analysed compositions (mol %) and measured densities

Sample	SiO_2	Al_2O_3	MgO	CaO	Na_2O	SO_3	ZnO	Dopant	Density (g/cm^3)
Base SLS (XRF)	70.51 (72.00)	0.59 (0.48)	5.48 (5.01)	9.25 (9.13)	13.95 (13.20)	0.22 (0.18)	0.00 (<0.10)	0.00 (<0.10)	2.484
TiO_2 SLS	70.31	0.59	5.48	9.25	13.95	0.22	0.00	0.20	2.490
ZrO_2 SLS	70.31	0.59	5.48	9.25	13.95	0.22	0.00	0.20	2.497
HfO_2 SLS	70.31	0.59	5.48	9.25	13.95	0.22	0.00	0.20	2.501
Nb_2O_5 SLS	70.31	0.59	5.48	9.25	13.95	0.22	0.00	0.20	2.504
Ta_2O_5 SLS	70.31	0.59	5.48	9.25	13.95	0.22	0.00	0.20	2.518
MoO_3 SLS	70.31	0.59	5.48	9.25	13.95	0.22	0.00	0.20	2.493
WO_3 SLS	70.31	0.59	5.48	9.25	13.95	0.22	0.00	0.20	2.510
Al_2O_3 SLS	66.10 (68.52)	5.00 (5.03)	5.48 (5.22)	9.25 (8.94)	13.95 (13.55)	0.22 (<0.10)	0.00 (<0.10)	0.00 (<0.10)	2.511
Al_2O_3 / TiO_2 SLS	65.90	5.00	5.48	9.25	13.95	0.22	0.00	0.20	2.513
Al_2O_3 / Nb_2O_5 SLS	65.90	5.00	5.48	9.25	13.95	0.22	0.00	0.20	2.522
ZnO SLS	70.51 (70.37)	0.59 (0.52)	4.48 (3.12)	9.25 (8.89)	13.95 (14.30)	0.22 (0.31)	1.00 (0.82)	0.00 (<0.10)	2.521
ZnO / TiO_2 SLS	70.31	0.59	4.48	9.25	13.95	0.22	1.00	0.20	2.523
ZnO / Nb_2O_5 SLS	70.31	0.59	4.48	9.25	13.95	0.22	1.00	0.20	2.521
0.01% Fe_2O_3	70.50	0.59	5.48	9.25	13.95	0.22	0.00	0.01	2.491
0.05% Fe_2O_3	70.46	0.59	5.48	9.25	13.95	0.22	0.00	0.05	2.492
0.10% Fe_2O_3	70.41	0.59	5.48	9.25	13.95	0.22	0.00	0.10	2.494

3. Results

Table 1 presents the nominal compositions of all studied glasses. The XRF analysis results for the base (undoped) glass are also presented; as are the measured densities for all glasses. As expected, densities of all doped glasses are slightly greater than the density of the base glass, reflecting the effects of the heavier added constituents on glass densities [33–35].

XRD patterns for three of the studied samples, representative of all of the studied glasses, are shown in Figure 3. All patterns are consistent with glasses, with no sharp diffraction peaks and a broad amorphous hump centred at ca. 25 $^{o}2\theta$. The doped systems were analysed through XRD to confirm no diffraction peaks were present (not presented). All diffraction patterns of the doped systems were the indishtinguable from that of the base glass, and confirm the X-ray amorphous nature of all samples.

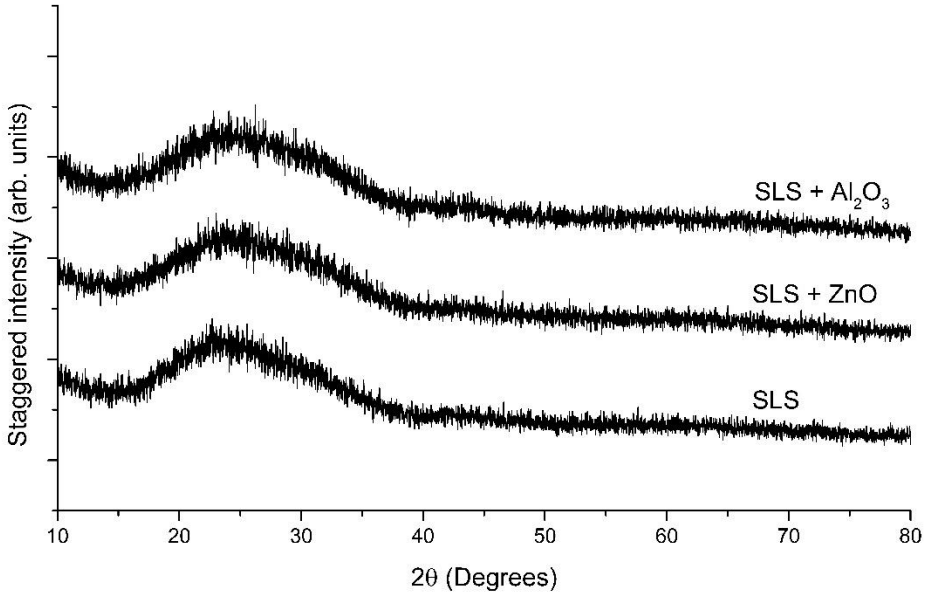

Figure 3. X-Ray diffraction patterns of undoped (base) glasses

Raman spectra of doped and undoped float glass samples are shown in

*Figure **4***. Each trace is composed of five main peaks, consistent with other float glass samples [33,34]. The Nb_2O_5 and MoO_3 doped samples have an additional peak as labelled by ● and ■ respectively. In Figure 4 the Nb_2O_5 doped sample displays an additional peak centered at 875cm^{-1} corresponding to NbO_6 octahedra [36,37], which have a higher Raman cross section relative to the glass matrix. $[MoO_3]^{2-}$ complexes in soda lime silicate glasses give rise to the peak at 925cm^{-1} [38,39]. The results indicate no major structural changes occur upon small modifications to the base glass matrix. This is consistent with the low doping levels and the XRD analyses in Figure 3.

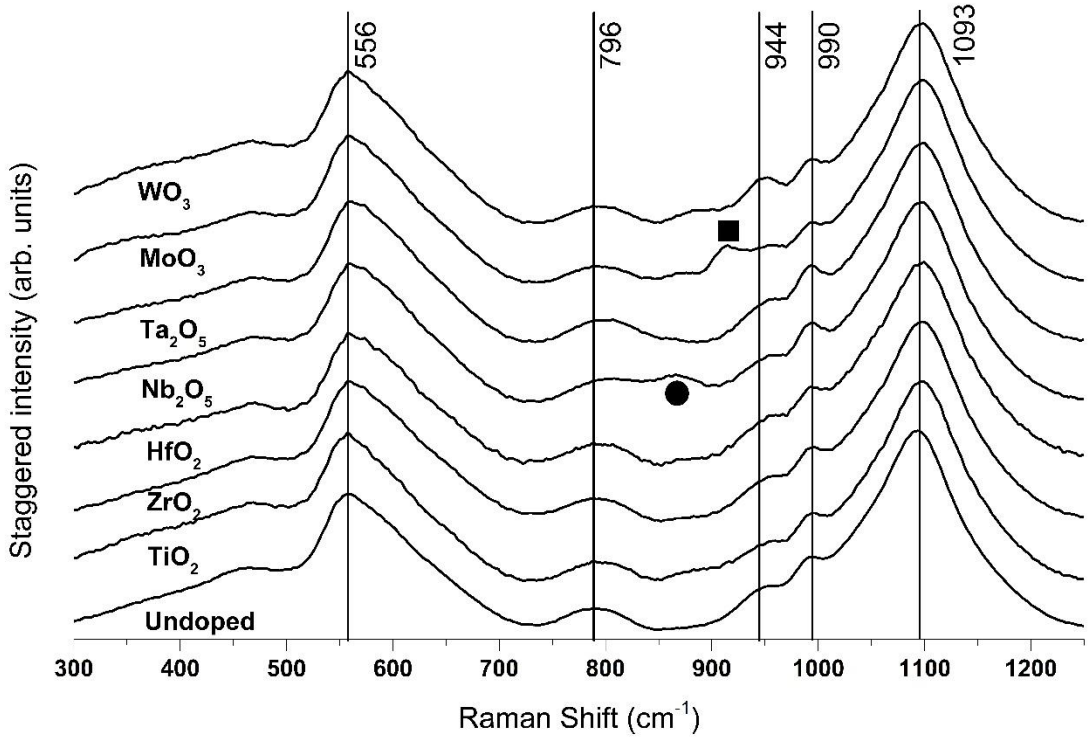

Figure 4. Normalised Raman spectra of base and doped glasses, ● = NbO_6 octahedra (875cm^{-1}), ■ = $[MoO_4]^{2+}$ tetrahedra (925cm^{-1})

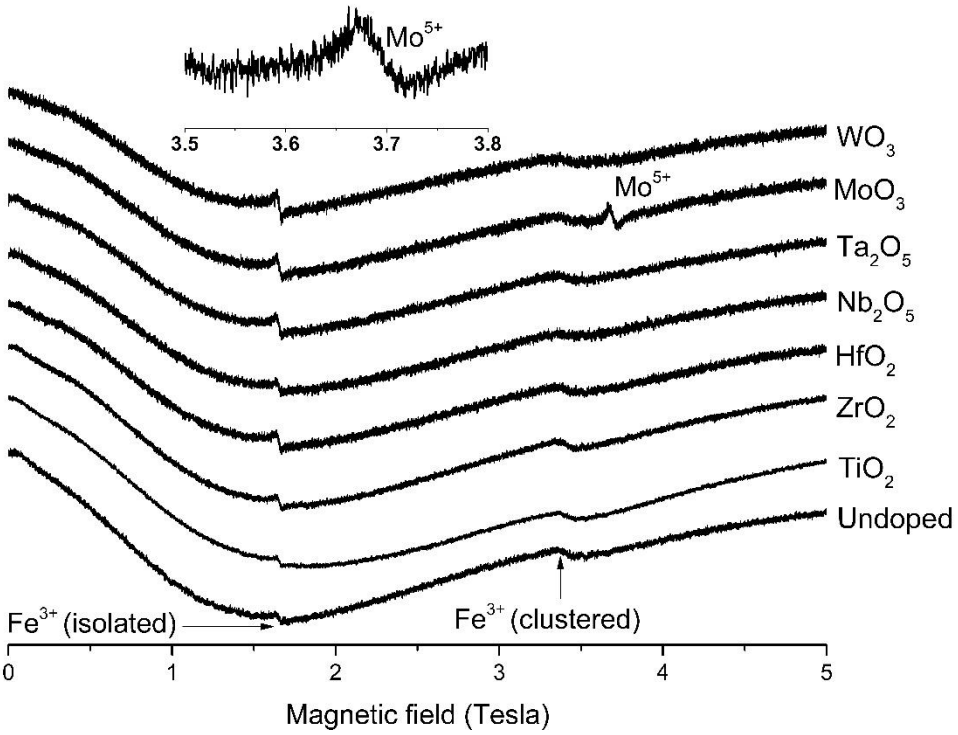

Figure 5. X-band EPR spectra of base SLS and doped glasses, inset is zoomed region between 3.5-3.8T for MoO_3 doped glass

Figure 5 shows EPR spectra of powdered glass samples, measured in silica tubes at X-band frequencies. Two paramagnetic signals, g=4.3 (1.6T) and g=2.0 (3.4T), correspond to Fe^{3+} in isolated and clustered environments respectively [40], though this is highly contensted. Whilst Mn^{2+} results in resonances at g=4.3 and g=2.0 [41,42], the lack of hyperfine structure at g=2.0 further indicates that the observed resonances are due to Fe^{3+}. Fe_2O_3 was not deliberately added to the glass melts and is present in impurity levels. Doped samples display the same peaks as the base glass, indicating the dopants are in the expected oxidation states of Ti^{4+}, Zr^{4+}, Hf^{4+}, Nb^{5+}, Ta^{5+}, W^{6+}, and Mo^{6+}. In the case of MoO_3 doped glass there is an additional weak resonance at g=1.92 (3.7T) corresponding to Mo^{5+}, shown in the inset of Figure 5.

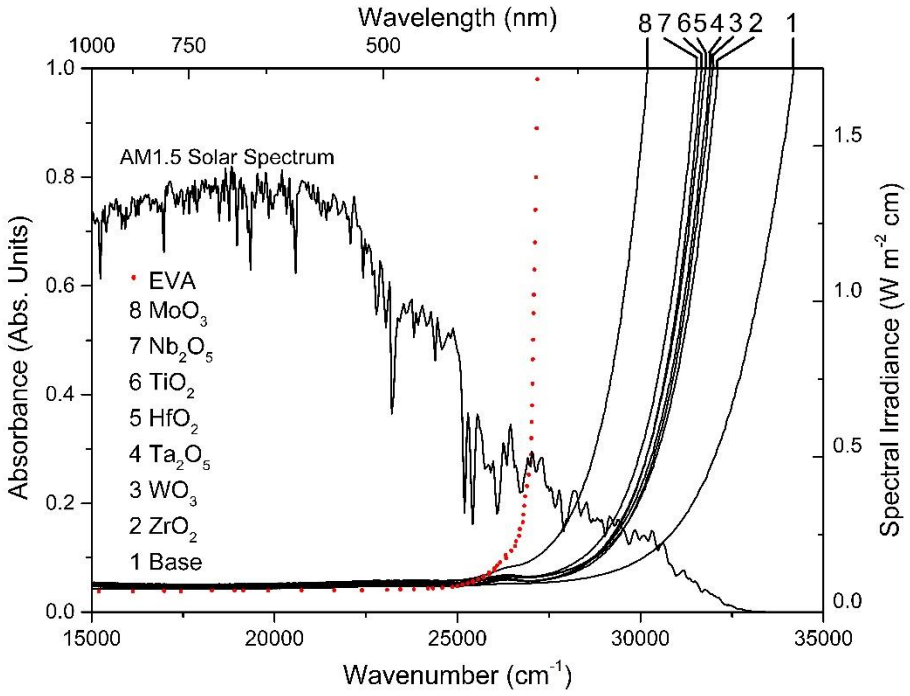

Figure 6. UV-VIS absorption of base and doped glasses

UV VIS absorption spectra of base and doped glasses are shown in Figure 6. These spectra all show strong UV absorption edges arising from the Si-O network and network modifying cations. Importantly this band is modified strongly by transition metals including Fe-O bonds. The MoO_3 doped spectra is 4,000cm^{-1} (~40nm) shifted towards the visible region relative to the base glass. The dotted line is reproduced from Yang *et al.* [43] and extended with data from Fix *et al.* [44], giving the absorbance of EVA glue. This value changes depending on the composition and age of the glue [45], with older, more irradiated glue having an absorption shifted towards the visible. The AM1.5 solar spectrum shows that high energy photons (>25,000cm^{-1}, <400nm) have lower spectral irradiance, however these photons are particularly damaging to the polymer layers. The UV absorption profiles of the doped glasses absorb significant portions of these high energy, damaging, photons, particulary in the case of MoO_3.

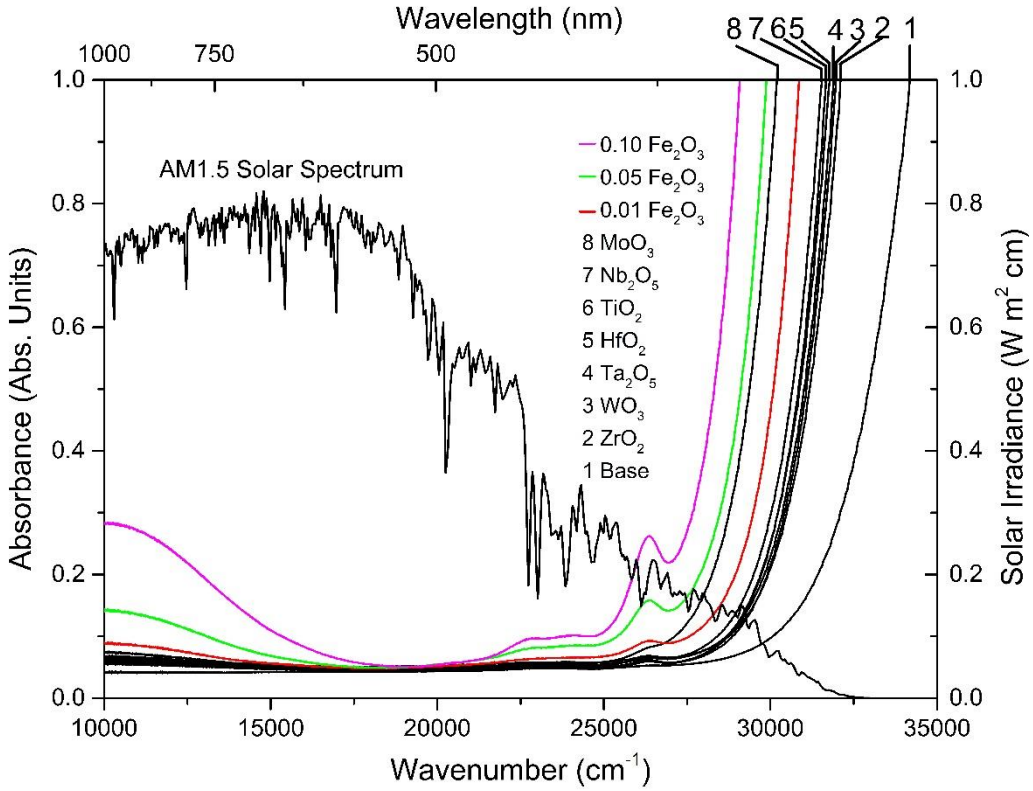

Figure 7 UV Vis IR absorbance of d^0 doped glasses and Fe_2O_3 doped glasses

Figure 7 shows UV Vis absorption spectra of the d^0 doped glasses, and Fe_2O_3 doped glasses. Increasing quantities of Fe_2O_3 in silicate glasses shift the UV edge towards the visible. The prominent peak at 26,220cm^{-1} (381nm) corresponds to the $^6A_1(S) \rightarrow {}^4E(D)$ transition of Fe^{3+} [9] which is present in all samples, in a lower intensity in the d^0 doped samples. MoO_3 doped SLS glass has a UV edge of similar position to that of 0.05mol% Fe_2O_3, with lower intensity of bands at 26,220cm^{-1} (381nm). Absorption in the IR region corresponds to Fe^{2+} [9] and prevents the transmission of photons close to the bandgap of c-Si solar cells, deleteriously impacting efficiency. All sample were 8.0±0.1mm thickness and were normalised to 10mm thickness.

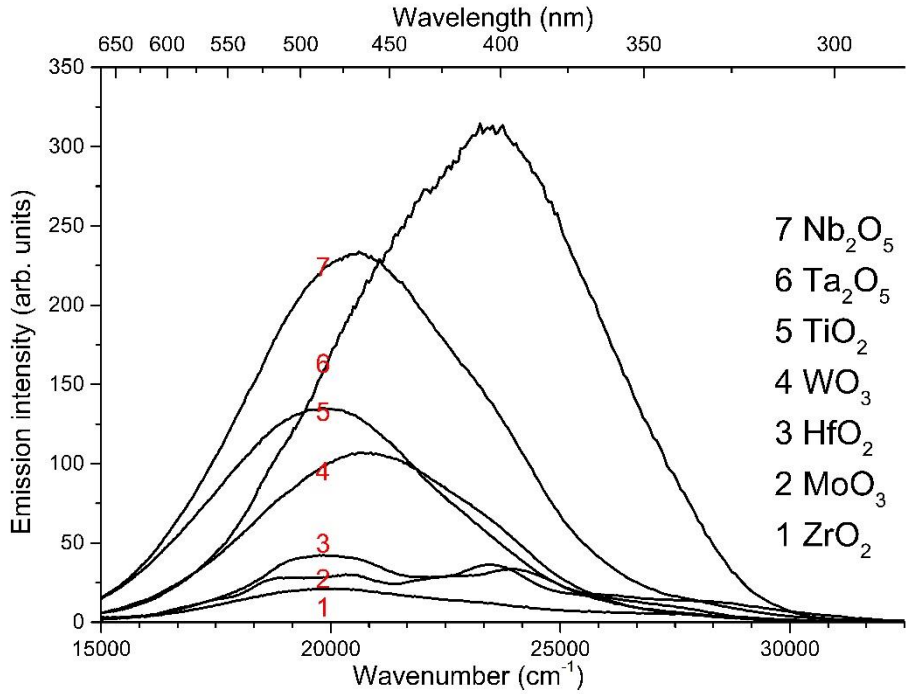

Figure 8. Fluorescence emission intensity under 41,666cm^{-1} (240nm) excitation (mercury discharge lamp)

The fluorescence emission spectra from 41,666cm^{-1} (240nm) excitation of d^0 doped glasses are presented in Figure 8**.** Each demonstrates broadband emission between 19,000cm^{-1} and 25,000cm^{-1} (400nm to 525nm). The colour photograph in Figure 10 shows the variation in colour and emission intensity upon UV excitation. ZrO_2 and MoO_3 doped glasses weakly emit at these excitation wavelengths [20]. Figure 9 shows the maximum intensity of emission at various excitation wavelengths, all dopants have stronger emission at higher wavenumber excitation. The glasses doped with Nb_2O_5 and Ta_2O_5 contain twice the quantity of active ions relative to TiO_2, ZrO_2, HfO_2, MoO_3 and WO_3. This may, in part, explain the greater emission intensity of the 0.20mol% doped SLS glasses with Nb_2O_5 and Ta_2O_5. Modification of the host matrix affects the emission of TiO_2 as presented in Figure 11, with the addition of 5.00mol% Al_2O_3 into the glass increasing emission intensity by a factor of 2. The effect is also present in Nb_2O_5 doped glasses with a modified matrix, the addition of 1.00mol% ZnO increases emission intensity by a factor of 2.5, as shown in Figure 12.

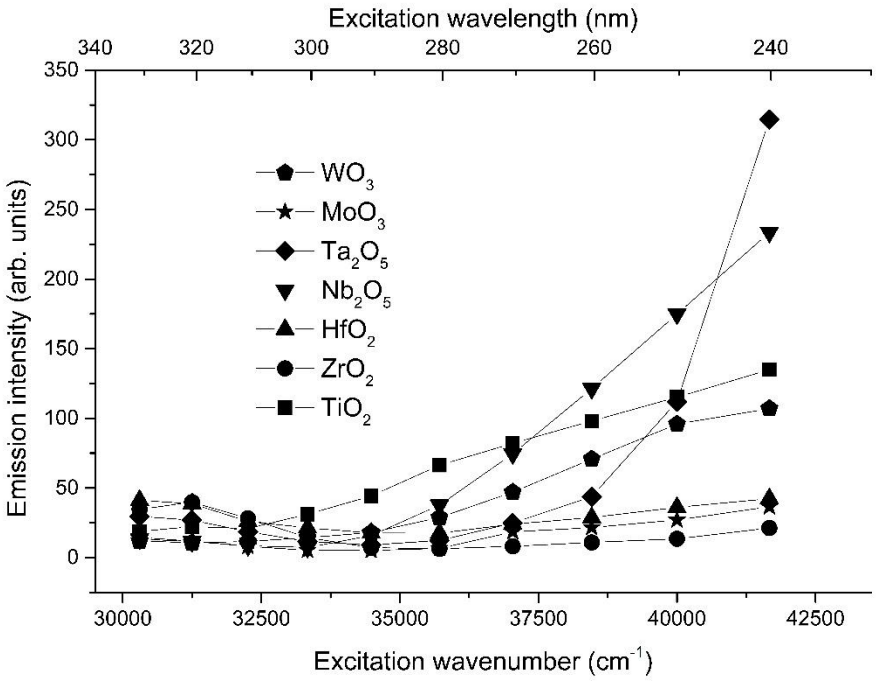

Figure 9. Variation of emission intensity as a function of excitation wavelength and dopant type.

Figure 10 shows the visible fluorescence from the singularly doped d^0 glasses. As sample thicknesses and an excitation beam size of $1cm^2$ are common to all samples and measurements, the total cross sectional area which is excited is consistent, minimising sample differences.While at sea level there are few photons with energies within the deep UV (≥ 33,000cm^{-1}, < 300nm) that would induce high fluorescence emission from the doped glasses, the effect, albiet at lower intensity, still occurs from excitation in the near UV region (33,000cm^{-1} to 30,300cm^{-1} or 300nm to 300nm).

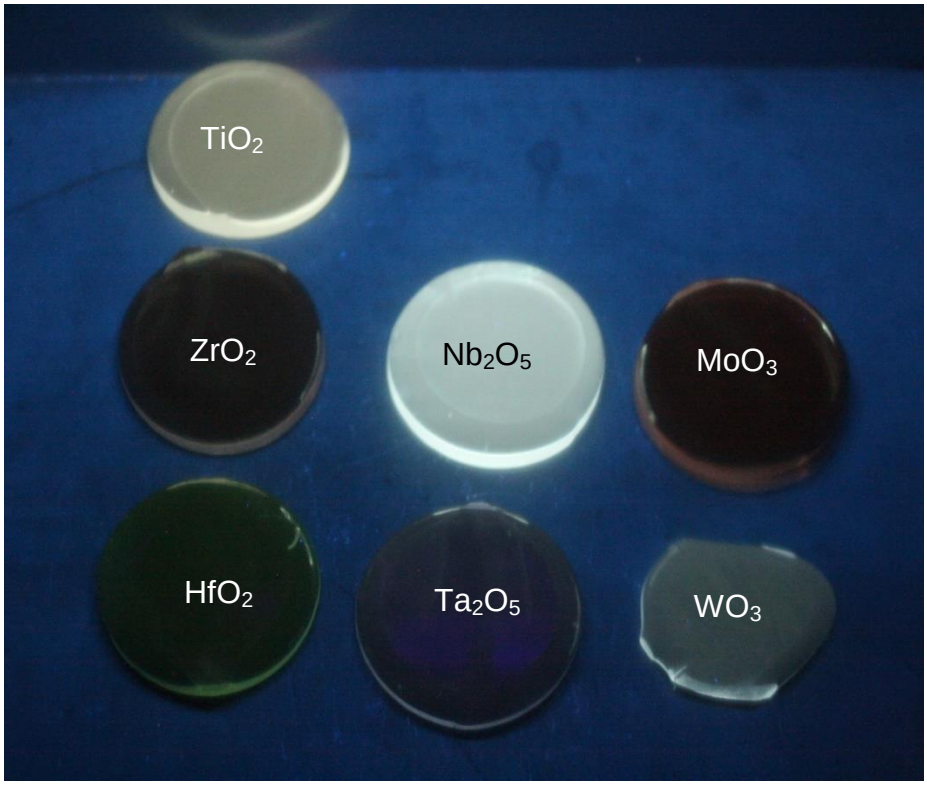

Figure 10. Visible fluorescence from d^0 doped SLS glasses. Photograph taken under 39370cm^{-1} (254nm) UV light.

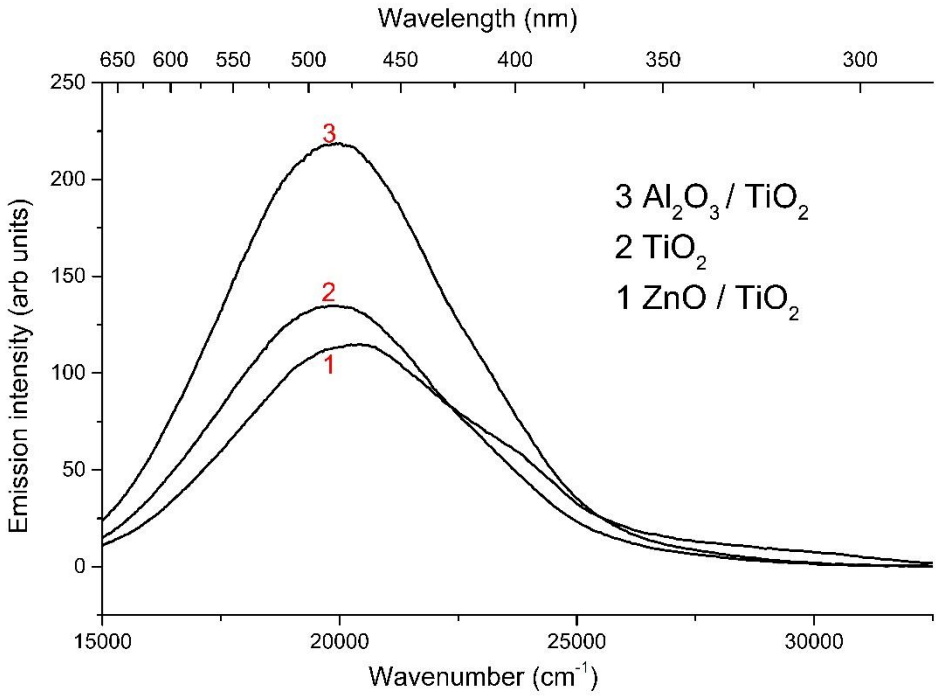

Figure 11. Fluorescence emission of doped TiO_2 glasses

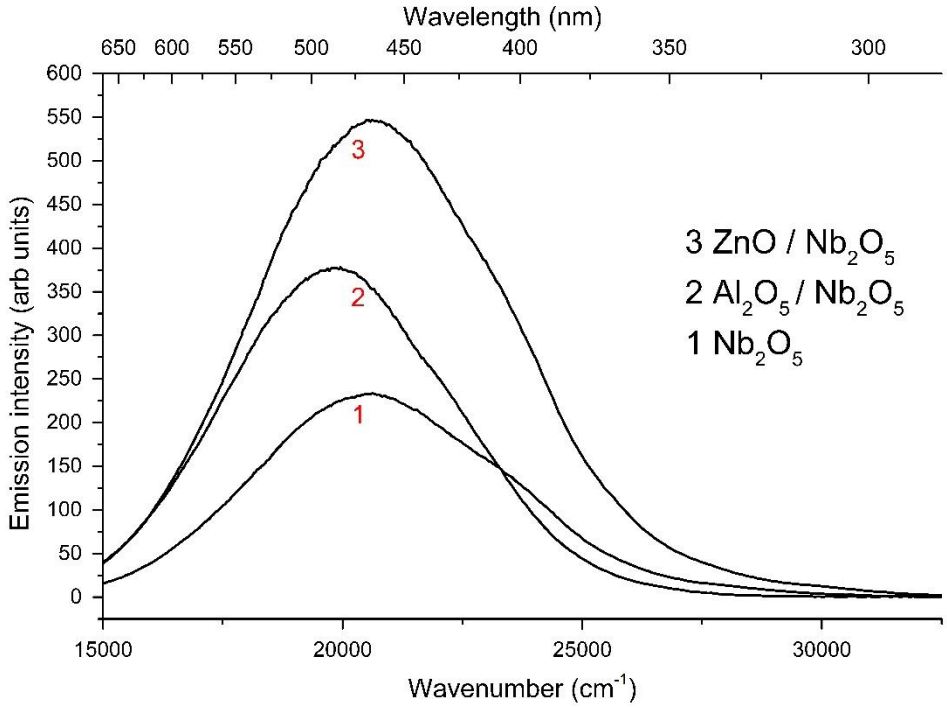

Figure 12. Fluorescence emission of doped Nb_2O_5 glasses

4. Discussion

The XRD patterns in Figure 3 show no sharp peaks or lines associated with crystalline phases, thus confirming the amorphous nature of the representative samples considered. The diffraction patterns are consistent with other oxide glasses, showing the amorphous "hump" typical of oxide glasses [46]. Whilst transition metal dopants can induce crystallisation in glass melts, the low doping concentrations in this study are below the thresholds observed in other studies [47,48]. Differences in the profile of XRD patterns are not readily detected in SLS glasses with increasing Al_2O_3 content below ca. 7.0mol% Al_2O_3 [49]. The replacement of SiO_2 with Al_2O_3 favours the formation of Q^3 structural units [50]. The amorphous nature of the glasses studied here reduces fluorescence intensities but broadens emission peaks, by comparison with crystalline equivalents [51]. Since both ZnO and Al_2O_3 demonstrate intermediate glass forming characteristics [46] they both can integrate and act as network formers. Densities are presented in Table 1 and are consistent with both the Fluegel model [33] and other experimental values [34], indicating that glass compositions, for all samples, are close to their nominal compositions based on batch calculations.

The Raman spectra in

Figure ***4*** show only small variations between the base and doped glasses, with only Nb_2O_5 and MoO_3 showing significant changes highlighted with the circle ● at 875cm^{-1} and the square ■ at 925cm^{-1} respectively. The six Raman bands in the base glass spectrum correspond to different structural motifs, the most intense band centred on 1093cm^{-1} is due to the stretching mode of Si-O-Si in Q^3 arrangements [52–55] indicating a highly polymerised silicate network. The broad band centred at 990cm^{-1} is consistent with the Si-NBO stretching mode (i.e. Q^2) [53,54]. The band centred at at ca. 944cm^{-1} is due to Q^2 speciation. The band centred at 796cm^{-1} arises from Si-O-Si symmetric stretching modes between Si-O tetrahedra [52,54,56]. The bands at 450cm^{-1} and 556cm^{-1} correspond to Si-O-Si symmetric stretching of Q^4 and Q^3 species, respectively [57]. The SLS glass sample doped with 0.20mol% Nb_2O_5 exhibits an extra band relative to the base glass, at around 875cm^{-1}. This is attributed to Nb-O symmetric vibrations in NbO_6 octahedra [58]: due to the high Raman cross section of niobium octahedra the peaks are detectable at low (>0.10mol%) concentrations in SLS glasses [36,37]. Molybdate tetrahedra also present strong Raman cross sections, thus giving rise to a stronger signal relative to the corresponding network [59]. The peak at 925 cm^{-1} in

Figure ***4*** corresponds to symmetric stretching of $[MoO_4]^{2-}$ tetrahedral entities in the glassy phase [38,39]. Bands associated with the d^0 transition metals, Ti^{4+} (937cm^{-1} corresponding to internal vibrations of TiO_4 tetrahedra, and 1100cm^{-1} to symmetric stretches of TiO_4) [60], Zr^{4+} (642cm^{-1} tetragonal ZrO_2) [58], Hf^{4+} (680cm^{-1} tetragonal HfO_2), Ta^{5+} (786cm^{-1} octahedral TaO_6) [61] and W^{6+} (916cm^{-1}, 958cm^{-1}, 1017cm^{-1} octahedral WO_6) [62], were expected due to their high polarisability relative to Si. However, these were not obsevered through a subtraction of the base glass spectrum from the doped glass' spectra. The high polarisability of the transition metals confer a higher Raman cross section relative to the silicate network, however, the low doping concentrations used may result in low intensity peaks which are not readily detected.

EPR detects unpaired electrons, hence the resonances at g=4.3 (1.6T) and g=2.0 (3.4T) shown in Figure 5 correspond to Fe^{3+} which occurs as an impurity in the raw materials used to produce all sample glasses. Both resonances have been widely observed, even in spectra for highly dilute glasses [40]. Fe^{2+} cannot be directly measured though room temperature X-band EPR due to its short spin-lattice relaxation time and lack of unpaired electrons [40]. The resonance at g=4.3 (1.6T) corresponds to Fe^{3+} in an isolated environment [41,63]. The resonance at g=2.0 (3.4T) is due to exchange-coupled Fe^{3+} ions [63–65]. It occurs even at impurity concentrations, but has also been attributed to octahedral Fe^{3+} [40,66]. Since EPR does not detect unpaired electrons and d^0 ions have no unpaired electrons, the lack of additional EPR peaks is consistent with the dopants being present in the expected oxidation states of Ti^{4+}, Zr^{4+}, Hf^{4+}, Nb^{5+}, Ta^{5+}, Mo^{6+} and W^{6+} [20,23,24] . However, the EPR spectrum for the MoO_3 doped glass (Figure 5) shows an additional weak resonance at g=1.92 (3.7T) which corresponds to Mo^{5+} [23]. This reduced form of Mo (d^1) can give rise to a yellow colour in oxide glasses due to the $^4A_2$-$^4T_2$ absorption band centred at 28,500 cm^{-1} (350nm) and 22,700 cm^{-1} (440nm) [23,67,68].This may partly explain the shifted UV edge in the optical absorption spectra shown in Figure 6. However, given the weakness of the Mo^{5+} EPR resonance, it can be concluded that the proportion of Mo present in this oxidation state is very small and the vast majority of Mo is present as Mo^{6+}. The oxidation state of Fe in soda lime silica glasses is affected by batch constituents and redox conditions during melting. The oxidation state/s of d^0 transition metal oxides dissolved in molten

glasses can thus be influenced / controlled by redox conditions, affecting the absorbance and emission properties of the glasses [23]. Redox control is essential for any commercial glass manufacture. Using current float glass manufacturing technologies, typical $Fe^{2+}/\Sigma Fe$ redox ratios of ~0.2 are common. Whilst the glasses produced in this study did not utilise commercial glassmaking raw materials or melting atmospheres, they were melted at broadly similar temperatures and thus, according to Van t'Hoff's Law, it is estimated that the $Fe^{2+}/\Sigma Fe$ redox ratios in the glasses studied were not greatly dissimilar to those obtained in many commercial float glasses, although it is likely they were more oxidised than float glasses. It was not possible to quantitatively measure the iron content from the EPR spectra as the measurements were made to qualitatively determine the valance of the dopants. The weakness of the Fe^{3+} resonances are qualitatively consistent with Fe^{3+} contents in the ppm range [69]. The Fe_2O_3 content was below the limit of detection for the program used for XRF (ca. 200ppm). For some of the dopants studied here (Ti, Mo), redox potentials developed by Schreiber et al [70,71] indicate that, under all but very strongly reducing conditions, these dopants will occur in soda-lime-silica glasses as Ti^{4+} and as, predominantly, Mo^{6+}. No comparable glass redox potential data was identified for the other dopants studied here, however, based on aqueous redox potentials it can reasonably be assumed that these dopants will occur in soda-lime-silica glasses prepared under oxidising melting conditions, predominantly as Nb^{5+}, Ta^{5+}, Zr^{4+}, Hf^{4+} and W^{6+}. The results of this study are consistent with this view.

Optical samples were polished to 8.0±0.1 mm thickness and, as shown by the transmission spectra in Figure 6, all are of high quality optical polishing as poor polishing leads to large amounts of scattering at the air-glass interface and results in poor transmission of light. The UV absorption edge is characterised by cut off wavelength corresponding to photon energies high enough to induce absorption [47]. In similar silicate glass compositions, Meng *et al.* showed that 1 mol % MoO_3 shifts UV absorption to lower wavenumbers more strongly than some other d^0 ions (Ti^{4+}, Zr^{4+}, Nb^{5+}, Ta^{5+} and W^{6+}) [20], and we find a corresponding result for the glasses studied here. It has been demonstrated the local structure of MoO_3 has a strong influence on the absorption which can shift the absorption edge towards ca. 24,000 cm^{-1} (415nm)

[72]. However, as shown by our EPR results and the corresponding optical absorption spectra, in the Mo-doped sample studied here, the molybdenum has been partially reduced to Mo^{5+} which could contribute to the shifted absorption. In Figure 7, Fe_2O_3 doped glasses are shown to shift the UV edge towards the visible region with increasing quantities of iron oxide. It has been demonstrated 0.01mol% Fe_2O_3 doped silicate glass as a PV encapsulant layer reduces module output by 1.1% due to the visible and IR absorptions at 26,220cm^{-1} and 11,000cm^{-1} (381nm and 909nm) of Fe^{3+} and Fe^{2+} [10]. Doping silicate glasses with 0.20mol% of d^0 ion oxide provides the solar protection, shown in Figure 6, without the deleterious bands shown in Figure 7.

EVA glues absorb strongly above 26,666cm^{-1} (below 375nm) [43] with photons of higher energy inducing greater damage. An NREL study on the yellowing index of EVA glues in silicon based PV panels covered with a standard SLS glass with a UV edge of 295nm was 81.9. PV modules prepared in the same manner with SLS glasses doped with cerium oxide to control the UV edge to 325nm and 330nm had yellowing indexes of 23.8 and 17.8 respectively after 35 weeks of accelerated aging [45]. The glasses in the NREL study were doped with cerium oxide: we postulate that the d^0 doped glasses studied here may also be suitable to achieve similar UV protection. As shown in Figure 6, glasses with UV absorption closer to that of the EVA absorption line do not act as 100% effective bandpass filters. Shifting the absorption of the glasses to overlap the EVA absorption would induce a deleterious effect on the module efficiency by absorbing visible photons. An effective balance of the beneficial UV absorption against the negative visible absorption in the glass superstrate requires further study.

As shown in Figure 8 under excitation from 41,666cm^{-1} (240nm) light, there is a large variation in emission intensity as a function of dopant type. The centre of the emission peaks vary up to 5,000cm^{-1} (100nm) between Ta_2O_5 and Nb_2O_5. At sea level there are few photons with high energies in the deep UV (> ca. 33,000 cm^{-1}, < 300nm), that would be required to induce strong fluorescence emission from glasses containing the dopants described herein. However, the effect, albeit weaker, still occurs from excitation in the near-UV region (ca. 33,000cm^{-1} to 30,300 cm^{-1} or 300 to 330 nm). It has been suggested a possible origin of the emission are from defects in the silicate network

induced by the addition of the various doped ions, especially Ta^{5+} [22], however, the EPR spectra only show Fe^{3+} impurity. A more convincing mechanism is ligand to metal charge transfer (LMCT) [73]. The excited state corresponds to nd^0 (n=3, 4, 5) of the transition metal ion, and the ground state is the $2p^6$ state of the oxide ions surrounding it, as shown in Figure 13.

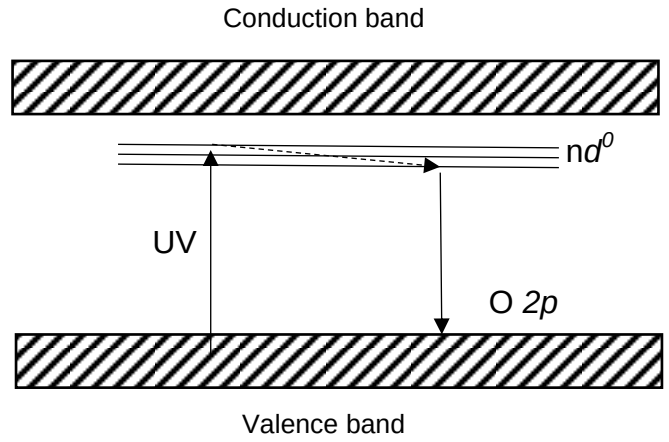

Figure 13 Schematic mechanism for nd^0 fluorescence emission n=3,4,5

In Figure 9 the variation of emission intensity as a function of excitation wavelength is shown. While at 41,666cm^{-1} (240nm) excitation the Ta_2O_5 doped sample shows the strongest emission, Nb_2O_5 and TiO_2 were selected for codoping with Al_2O_3 and ZnO, in an effort to further increase emission intensity, due to their low cost and high emission intensities over a wide range of excitation ranges. The levels of Nb_2O_5 and Ta_2O_5 added contained twice the quantity of active ions relative to the remaining doped systems. Due, at least in part, to the effectively higher doping concentration, the emission intensity is proportionately higher. The glasses were modified to either contain 5.0 mol% Al_2O_3 (replacing SiO_2), or 1.0 mol% ZnO (replacing MgO). Shown in Figure 11, the Al_2O_3 codoped TiO_2 sample exhibits enhanced fluorescence emission without changing λ_{max} due to the matrix having lower total phonon energy [74], resulting in fewer non-radiative losses, and thus a higher fluorescence emission. ZnO codoped glasses induce to a shoulder peak developing around 23,000cm^{-1} (434nm). This is due to the fluorescence emission of Zn^{2+}, it is understood the luminescence is due to interstitial

zinc defects, involving a transition from the conduction band edge to a deep acceptor level [75]. It has been shown that codoping with ZnO/Nb_2O_5 enhances the fluorescence emission relative to singly-doped Nb_2O_5 samples [76].This may be due to enhancing the electron-hole recombination effect. Small modifications to the host glass matrix do not significantly change the structure structure, as evidenced by the XRD and Raman traces, but can have a significant effect on the emission intensity when excited under UV light. Differences in the Raman spectra reflect the high polarisability of the transition metal dopants. Glasses outlined in this article would be particularly suitable for PV modules in locations with high UV such as high altitude locations such as Peru, Chile, Argentina or New Zealand where the EVA and backsheet are more vunerable and the higher flux of UV photons allows for greater emission intensities.

5. Conclusions

A series of glasses doped with d^0 ions was prepared through a standard melt quench technique. Upon excitation by UV light all glasses demonstrate visible fluorescence of different magnitudes centred between 20,000cm^{-1} and 25,000cm^{-1} (400nm – 500nm), with the greatest intensity from 41,666cm^{-1} (240nm) excitation. A shift in the absorption spectra towards the visible region has been demonstrated in all doped samples, with MoO_3 doped glass having the strongest effect. This has been attributed to a partial reduction in Mo^{6+} to Mo^{5+} shown by the peak at g=1.92 (3.7T) through EPR. Glasses doped with Nb_2O_5 and MoO_3 exhibit additional Raman peaks centred at 875cm^{-1} and 925cm^{-1}, respectively, attributed to Nb-O vibrations in NbO_6 octahedra and Mo-O stretching modes in $[MoO_4]^{2-}$ tetrahedra. Through modification of the glass matrix with Al_2O_3 or ZnO, the fluorescence emission intensity can be enhanced in the case of TiO_2 and Nb_2O_5. SLS glasses doped with d^0 ions confer several potential advantages for PV cover glass applications through absorption of damaging UV light and re-emission as near-UV and visible light, which could simultaneously enhance both PV module lifetimes and efficiencies. The glasses presented in this article are primarily suitable for

absorption of damaging UV photons and hence for the protection of the EVA glue and backsheet layers. Further optimisation is required to fully overlap the absorption profile of the glass cover sheet to that of the EVA glue, whilst remaining transparent to visible photons. Modification of the excitation and emission properties of the dopants to more closely align with that of the particular solar cell is also required.

Acknowledgements

BLA and PAB acknowledge with thanks EU FP7 Solar-Era Net (Project Solareranet-0005), the Technology Strategy Board (Programme 620086) and Solar Capture Technologies Ltd for funding. The authors also thank Jonathan Booth, Ian Baistow, Robin Orman, Simon Johnson, Stefan Karlsson, Christina Ståhlhandske, Peter Sundberg and Anne Andersson for useful discussions. We would also like to thank the two anonymous reviewers for their helpful comments.

References

[1] C.L. Kwan, Influence of local environmental, social, economic and political variables on the spatial distribution of residential solar PV arrays across the United States, Energy Policy. 47 (2012) 332–344. doi:10.1016/j.enpol.2012.04.074.

[2] G. Conibeer, Third-generation photovoltaics, Mater. Today. 10 (2007) 42–50. doi:10.1016/S1369-7021(07)70278-X.

[3] F. Liu, L. Jiang, S. Yang, Ultra-violet degradation behavior of polymeric backsheets for photovoltaic modules, Sol. Energy. 108 (2014) 88–100. doi:10.1016/j.solener.2014.06.027.

[4] J.M. Kuitche, R. Pan, G. Tamizhmani, Investigation of dominant failure mode(s) for field-aged crystalline silicon PV modules under desert climatic conditions, IEEE J. Photovoltaics. 4 (2014) 814–826. doi:10.1109/JPHOTOV.2014.2308720.

[5] D. Jordan, S. Kurtz, Photovoltaic module stability and reliability, Elsevier Ltd., 2016. doi:10.1016/B978-1-78242-336-2.00003-3.

[6] N. Kim, S. Lee, X.G. Zhao, D. Kim, C. Oh, H. Kang, Reflection and durability study of different types of backsheets and their impact on c-Si PV module performance, Sol. Energy Mater. Sol. Cells. 146 (2016) 91–98. doi:10.1016/j.solmat.2015.11.038.

[7] F. Pern, Ethylene vinyl acetate (EVA) encapsulants for photovoltaic modules: Degradation and discoloration mechanisms and formulation modifications for improved, Die Angew. Makromol. Chemie. 252 (1997) 195–216. doi:10.1002/apmc.1997.052520114.

[8] A. Jentsch, K.J. Eichhorn, B. Voit, Influence of typical stabilizers on the aging behavior of EVA foils for photovoltaic applications during artificial UV-weathering, Polym. Test. 44 (2015) 242–247. doi:10.1016/j.polymertesting.2015.03.022.

[9] T.T. Volotinen, J.M. Parker, P.A. Bingham, Concentrations and site partitioning of Fe^{2+} and Fe^{3+} ions in a soda-lime-silica glass obtained by optical absorbance spectroscopy, Phys. Chem. Glas. Eur. J. Glas. Sci. Technol. Part B. 49 (2008) 258–270.

[10] M.R. Vogt, H. Hahn, H. Holst, M. Winter, C. Schinke, M. Kontges, R. Brendel, P.P. Altermatt, Measurement of the optical constants of soda-lime glasses in dependence of iron content and modeling of iron-related power losses in crystalline Si solar cell modules, IEEE J. Photovoltaics. 6 (2016) 111–118. doi:10.1109/JPHOTOV.2015.2498043.

[11] N.J. Ekins-Daukes, Routes to high efficiency photovoltaic power conversion, 2013 IEEE 39th Photovolt. Spec. Conf. (2013) 0013–0016. doi:10.1109/PVSC.2013.6744088.

[12] W. Shockley, H.J. Queisser, Detailed balance limit of efficiency of p-n junction solar cells, J. Appl. Phys. 32 (1961) 510–519. doi:10.1063/1.1736034.

[13] V. Badescu, A. De Vos, A.M. Badescu, A. Szymanska, Improved model for solar cells with down-conversion and down-shifting of high-energy photons, J. Phys. D-Applied Phys. 40 (2007) 341–352. doi:10.1088/0022-3727/40/2/009.

[14] W.G. van Sark, J. de Wild, J.K. Rath, A. Meijerink, R.E. Schropp, Upconversion in solar cells., Nanoscale Res. Lett. 8 (2013) 81. doi:10.1186/1556-276X-8-81.

[15] B.C. Rowan, L.R. Wilson, B.S. Richards, Advanced material concepts for luminescent solar concentrators, IEEE J. Sel. Top. Quantum Electron. 14 (2008) 1312–1322. doi:10.1109/JSTQE.2008.920282.

[16] M.X. Façanha, J.P.C. do Nascimento, M. a. S. Silva, M.C.C. Filho, a. N.. Marques, a. G. Pinheiro, a. S.B. Sombra, Up-conversion emission of Er^{3+}/Yb^{3+} co-doped $BaBi_2Nb_2O_9$ (BBN) phosphors, J. Lumin. 183 (2017) 102–107. doi:10.1016/j.jlumin.2016.08.011.

[17] U. Rambabu, S.-D. Han, Synthesis and luminescence properties of broad band greenish-yellow emitting $LnVO_4$:Bi^{3+} and (Ln_1, Ln_2)VO_4:Bi^{3+} (Ln=La, Gd and Y) as down conversion phosphors, Ceram. Int. 39 (2013) 701–708. doi:10.1016/j.ceramint.2012.06.081.

[18] R.L. Leonard, S.K. Gray, S.D. Albritton, L.N. Brothers, R.M. Cross, A.N. Eastes,

H.Y. Hah, H.S. James, J.E. King, S.R. Mishra, J.A. Johnson, Rare earth doped downshifting glass ceramics for photovoltaic applications, J. Non. Cryst. Solids. 366 (2013) 1–5. doi:10.1016/j.jnoncrysol.2013.01.029.

[19] B.C. Jamalaiah, M. Jayasimhadri, G.V.L. Reddy, Blue emitting $YAl_3(BO_3)_4:Tm^{3+}$ single-phase phosphors under UV excitation, Phys. Chem. Glas. Eur. J. Glas. Sci. Technol. Part B. 57 (2016) 68–70. doi:10.13036/17533562.57.2.008.

[20] X. Meng, S. Murai, K. Fujita, K. Tanaka, Intense visible emissions from d0 ions-doped silicate glasses, J. Ceram. Soc. Japan. 116 (2008) 1147–1149. doi:10.2109/jcersj2.116.1147.

[21] X. Meng, K. Tanaka, K. Fujita, S. Murai, Intense greenish emission from d0 transition metal ion Ti^{4+} in oxide glass, Appl. Phys. Lett. 90 (2007) 3–6. doi:10.1063/1.2437074.

[22] X. Meng, S. Murai, K. Fujita, K. Tanaka, Intense blue emission from tantalum-doped silicate glass, Appl. Phys. Lett. 89 (2006) 11–14. doi:10.1063/1.2335394.

[23] D. Möncke, D. Ehrt, Photoinduced redox reactions in Zr, Nb, Ta, Mo, and W doped glasses, Phys. Chem. Glas. Eur. J. Glas. Sci. Technol. Part B. 48 (2007) 317–323.

[24] D. Ehrt, Photoluminescence in the UV–VIS region of polyvalent ions in glasses, J. Non. Cryst. Solids. 348 (2004) 22–29. doi:10.1016/j.jnoncrysol.2004.08.121.

[25] D. Ehrt, Phosphate and fluoride phosphate optical glasses — properties , structure and applications, Phys. Chem. Glas. Eur. J. Glas. Sci. Technol. B. 56 (2015) 217–234. doi:10.13036/17533562.56.6.217.

[26] D. Ehrt, Photoluminescence in glasses and glass ceramics, IOP Conf. Ser. Mater. Sci. Eng. 2 (2009) 12001. doi:10.1088/1757-899X/2/1/012001.

[27] D. Ehrt, M. Leister, A. Matthai, Polyvalent elements iron, tin and titanium in silicate, phosphate and fluoride glasses and melts, Phys. Chem. Glas. 42 (2001) 231–239.

[28] M. Wiegel, G. Blasse, R. Feigelson, Luminescence of stoichiometric lithium niobate crystals, Mater. Res. Bull. 28 (1993) 1025–1028.

[29] M. Wiegel, G. Blasse, M. Ouwerkerk, Luminescence of potassium lithium niobate compositions, Mater. Res. Bull. 27 (1992) 617–621.

[30] M. Wiegel, W. Middel, G. Blasse, Influence of ns2 ions on the luminescence of niobates and tantalates, J. Mater. Chem. 5 (1995) 981–983. http://dx.doi.org/10.1039/JM9950500981.

[31] W.J. Schipper, J.J. Piet, H.J. De Jager, G. Blasse, On the luminescence of hafnium compounds, Mater. Res. Bull. 29 (1994) 23–30. doi:10.1016/0025-5408(94)90101-5.

[32] M. Wiegel, M. Hamoumi, Luminescence and nonlinear niobates and titanates optical properties of perovskite like niobates and titanates, Mater. Chem. Phys. 36 (1994) 289–293.

[33] A. Fluegel, Global Model for Calculating Room-Temperature Glass Density from the composition, J. Am. Ceram. Soc. 2625 (2007) 2622–2625. doi:10.1111/j.1551-2916.2007.01751.x.

[34] E. Kilinc, R.J. Hand, Mechanical properties of soda–lime–silica glasses with varying alkaline earth contents, J. Non. Cryst. Solids. 429 (2015) 190–197. doi:10.1016/j.jnoncrysol.2015.08.013.

[35] R. Limbach, S. Karlsson, G. Scannell, R. Mathew, M. Edén, L. Wondraczek, The effect of TiO_2 on the structure of Na_2O-CaO-SiO_2 glasses and its implications for thermal and mechanical properties, J. Non. Cryst. Solids. 471 (2017) 6–18. doi:10.1016/j.jnoncrysol.2017.04.013.

[36] A. Kaur, A. Khanna, V.G. Sathe, F. Gonzalez, B. Ortiz, Optical, thermal, and structural properties of Nb_2O_5 –TeO_2 and WO_3 –TeO_2 glasses, Phase Transitions. 86 (2013) 598–619. doi:10.1080/01411594.2012.727998.

[37] F.J. Caixeta, F.T. Aquino, R.R. Pereira, R.R. Goncalves, Broad and intense NIR luminescence from rare earth doped SiO_2-Nb_2O_5 glass and glass ceramic prepared by a new sol gel route, J. Lumin. 171 (2016) 63–71. doi:10.1016/j.jlumin.2015.08.054.

[38] N. Chouard, D. Caurant, O. Majérus, N. Guezi-Hasni, J.L. Dussossoy, R. Baddour-Hadjean, J.P. Pereira-Ramos, Thermal stability of SiO_2-B_2O_3-Al_2O_3-Na_2O-CaO glasses with high Nd_2O_3 and MoO_3 concentrations, J. Alloys Compd. 671 (2016) 84–99. doi:10.1016/j.jallcom.2016.02.063.

[39] N. Chouard, D. Caurant, O. Majerus, J.L. Dussossoy, S. Klimin, D. Pytalev, R. Baddour-Hadjean, J.P. Pereira-Ramos, Effect of MoO_3, Nd_2O_3, and RuO_2 on the crystallization of soda lime aluminoborosilicate glasses, J. Mater. Sci. 50 (2015) 219–241. doi:10.1007/s10853-014-8581-9.

[40] V. Vercamer, G. Lelong, H. Hijiya, Y. Kondo, L. Galoisy, G. Calas, Diluted Fe^{3+} in silicate glasses: Structural effects of Fe-redox state and matrix composition. An optical absorption and X-band/Q-band EPR study, J. Non. Cryst. Solids. 428 (2015) 138–145. doi:10.1016/j.jnoncrysol.2015.08.010.

[41] D.L. Griscom, Electron spin resonance in glasses, J. Non. Cryst. Solids. 40 (1980) 211–272. doi:10.1016/0022-3093(80)90105-2.

[42] J. Kliava, EPR of Impurity Ions in Disordered Soilds, Phys. Stat. Sol. B. 134 (1986) 411–455. doi:10.1002/pssb.2221340202.

[43] J. Yang, D. Lee, D. Baek, D. Kim, J. Nam, P. Huh, Effect of various encapsulants for frameless glass to glass Cu(In,Ga)$(Se,S)_2$ photovoltaic module, RSC Adv. 5

(2015) 51258–51262. doi:10.1039/C5RA03663A.

[44] T. Fix, A. Nonat, D. Imbert, S. Di Pietro, M. Mazzanti, A. Slaoui, L.J. Charbonniere, Enhancement of silicon solar cells by downshifting with Eu and Tb coordination complexes, Prog. Photovolt Res. Appl. (2016). doi:10.1002/pip.

[45] W.W. Holley, S.C. Agro, Advanced EVA-Based Encapsulants, NREL Rep. (1998) 1–95.

[46] Z.-H.H. Jiang, Q.-Y.Y. Zhang, The structure of glass: A phase equilibrium diagram approach, Prog. Mater. Sci. 61 (2014) 144–215. doi:10.1016/j.pmatsci.2013.12.001.

[47] Z. Wang, L. Cheng, Effects of doping CeO_2/TiO_2 on structure and properties of silicate glass, J. Alloys Compd. 597 (2014) 167–174. doi:10.1016/j.jallcom.2014.01.232.

[48] N. Ghaebi Panah, B. Eftekhari Yekta, V. Marghussian, E. Mohaghegh, Effects of TiO_2 and P_2O_5 on solarization and crystallisation of photosensitive lithium silicate glass, J. Non. Cryst. Solids. 430 (2015) 25–30. doi:10.1016/j.jnoncrysol.2015.09.018.

[49] Y. Fujimoto, Local structure of the infrared bismuth luminescent center in bismuth-doped silica glass, J. Am. Ceram. Soc. 93 (2010) 581–589. doi:10.1111/j.1551-2916.2009.03419.x.

[50] E.I. Kamitsos, J.A. Kapoutsis, H. Jain, C.H. Hsieh, Vibrational study of the role of trivalent ions in sodium trisilicate glass, J. Non. Cryst. Solids. 171 (1994) 31–45. doi:10.1016/0022-3093(94)90030-2.

[51] J.A. Duffy, Bonding, energy levels and bands in inorganic solids, Harlow : Longman Scientific and Technica, 1990.

[52] M. Wang, J. Cheng, M. Li, F. He, Raman spectra of sodalimesilicate glass doped with rare earth, Phys. B Condens. Matter. 406 (2011) 3865–3869. doi:10.1016/j.physb.2011.07.014.

[53] P. González, J. Serra, S. Liste, S. Chiussi, B. León, M. Pérez-Amor, Raman spectroscopic study of bioactive silica based glasses, J. Non. Cryst. Solids. 320 (2003) 92–99. doi:10.1016/S0022-3093(03)00013-9.

[54] F.L. Galeener, Band limits and the vibrational spectra of tetrahedral glasses, Phys. Rev. B. 19 (1979) 4292–4297. doi:10.1103/PhysRevB.19.4292.

[55] H. Aguiar, J. Serra, P. González, B. León, Structural study of sol-gel silicate glasses by IR and Raman spectroscopies, J. Non. Cryst. Solids. 355 (2009) 475–480. doi:10.1016/j.jnoncrysol.2009.01.010.

[56] A.K. Yadav, P. Singh, A review of the structures of oxide glasses by Raman spectroscopy, RSC Adv. 5 (2015) 67583–67609. doi:10.1039/C5RA13043C.

[57] T. Deschamps, C. Martinet, J.L. Bruneel, B. Champagnon, Soda-lime silicate glass under hydrostatic pressure and indentation: a micro-Raman study., J. Phys. Condens. Matter. 23 (2011) 35402. doi:10.1088/0953-8984/23/3/035402.

[58] D. Möncke, R. Ehrt, D. Palles, I. Efthimiopoulos, E.I. Kamitsos, M. Johannes, A multi technique study of a new lithium disilicate glass-ceramic spray-coated on ZrO_2 substrate for dental restoration, Biomed. Glas. 3 (2017) 41–55. doi:10.1515/bglass-2017-0004.

[59] D.A. McKeown, H. Gan, I.L. Pegg, W.C. Stolte, I.N. Demchenko, X-ray absorption studies of chlorine valence and local environments in borosilicate waste glasses, J. Nucl. Mater. 408 (2011) 236–245. doi:10.1016/j.jnucmat.2010.11.035.

[60] S. Richter, D. Möncke, F. Zimmermann, E.I. Kamitsos, L. Wondraczek, A. Tünnermann, S. Nolte, Ultrashort pulse induced modifications in ULE - from nanograting formation to laser darkening, Opt. Mater. Express. 5 (2015) 1834. doi:10.1364/OME.5.001834.

[61] G.M. De Pietro, C. Pereira, R.R. Gonçalves, S.J.L. Ribeiro, C.D. Freschi, F.C. Cassanjes, G. Poirier, Thermal, Structural, and Crystallization Properties of New Tantalum Alkali-Germanate Glasses, J. Am. Ceram. Soc. 98 (2015) 2086–2093. doi:10.1111/jace.13555.

[62] L. Bih, M. Azrour, B. Manoun, M.P.F. Graça, M.A. Valente, Raman spectroscopy, X-Ray, SEM, and DTA analysis of alkali-phosphate glasses containing WO_3 and Nb_2O_5, J. Spectrosc. 1 (2013). doi:10.1155/2013/123519.

[63] T. Castner Jr., G.S. Newell, W.C. Holton, C.P. Slichter, Note on the paramagnetic resonance of iron in glass, J. Chem. Phys. 32 (1960) 668–673. doi:10.1063/1.1730779.

[64] P. A. Bingham, J.M. Parker, T. Searle, J.M. Williams, I. Smith, Novel structural behaviour of iron in alkali – alkaline-earth – silica glasses, C.R. Cnimie. 5 (2002) 787–796. doi:10.1016/S1631-0748(02)01444-3.

[65] R.D. Dowsing, Electron Spin Resonance of High-Spin d5 Systems, J. Chem. Phys. 52 (1970) 2795. doi:10.1063/1.1673393.

[66] B. Camara, H.J. Oel, Behaviour and effect of iron in X-ray irradiated silicate glass, J. Non. Cryst. Solids. 65 (1984) 161–176. doi:10.1016/0022-3093(84)90363-6.

[67] P. S, G. S, S. J, N, Effect of composition and temperature on the absorption and emission spectra of molybdenum in glasses, J. Non. Cryst. Solids. 20 (1976) 1–14.

[68] G. Boulon, B. Moine, J. Bourcet, Spectroscopic properites of $^3P_1$ and $^3P_0$ excited states of Bi^{3+} ions in germanate glass, Phys. Rev. B. 22 (1980) 1163–1169.

[69] A. Elvers, R. Weismann, ESR spectroscopy - an analytical tool for the glass industry, Glas. Sci. Technol. Glas. Berichte. 74 (2001).

[70] H.D. Schreiber, N.R. Wilk, C.W. Schreiber, Comprehensive electromotive force series of redox couples in soda-lime-silicate glass, J. Non. Cryst. Solids. 253 (1999) 68–75. doi:10.1016/S0022-3093(99)00344-0.

[71] H.D. Schreiber, Redox processes in glass-forming melts, J. Non. Cryst. Solids. 84 (1986) 129–141. doi:10.1016/0022-3093(86)90770-2.

[72] R.S. Weber, Effect of Local Structure on the UV-Visible Absorption Edges of Molybdenum Oxide Clusters and Supported Molybdenum Oxides, J. Catal. 151 (1995) 470–474. doi:http://dx.doi.org/10.1006/jcat.1995.1052.

[73] P.D. Rack, M.D. Potter, S. Kurinec, W.H. Park, J. Penczek, B.K. Wagner, C.J. Summers, Luminescence properties of thin film $Ta_2Zn_3O_8$ and Mn doped $Ta_2Zn_3O_8$, J. Appl. Phys. 84 (1998) 4466–4470. doi:10.1063/1.368672.

[74] J. Zhao, X. Zheng, E.P. Schartner, P. Ionescu, R. Zhang, T.-L. Nguyen, D. Jin, H. Ebendorff-Heidepriem, Upconversion Nanocrystal-Doped Glass: A New Paradigm for Photonic Materials, Adv. Opt. Mater. (2016) 1–11. doi:10.1002/adom.201600296.

[75] L. Irimpan, V.P.N. Nampoori, P. Radhakrishnan, A. Deepthy, B. Krishnan, Size dependent fluorescence spectroscopy of nanocolloids of ZnO, J. Appl. Phys. 102 (2007). doi:10.1063/1.2778637.

[76] S.M. Lam, J.C. Sin, I. Satoshi, A.Z. Abdullah, A.R. Mohamed, Enhanced sunlight photocatalytic performance over Nb_2O_5/ZnO nanorod composites and the mechanism study, Appl. Catal. A Gen. 471 (2014) 126–135. doi:10.1016/j.apcata.2013.12.001.